



ZnO/rGO/C composites derived from metal–organic framework as advanced anode materials for Li-ion and Na-ion batteries

Yuan Wang¹, Qijiu Deng², Weidong Xue¹, Zou Jian¹, Rui Zhao^{1,*} , and Juanjuan Wang²

¹Institute of Applied Electrochemistry, Institute of Microelectronic and Solid State Electronic, University of Electronic Science and Technology of China, Chengdu 610054, People's Republic of China

²School of Materials Science and Engineering, Xi'an University of Technology (XAUT), Xi'an 710048, People's Republic of China

Received: 30 October 2017

Accepted: 4 January 2018

Published online:
12 January 2018

© Springer Science+Business
Media, LLC, part of Springer
Nature 2018

ABSTRACT

A novel ZnO/reduced graphene oxide/carbon (ZnO/rGO/C) composite is synthesized by pyrolysis of Zn-based metal–organic framework where graphene oxide and the glucose are imported as carbon sources. As a result, ZnO nanoparticles dispersing on a uniform reduced graphene sheet with a thin carbon layer construct a unique structure, which can prevent the aggregation of ZnO, enhance the electronic conductivity, and offer a robust scaffold during electrochemical processes. Compared to the bare ZnO and ZnO/rGO, the obtained ZnO/rGO/C composite can exhibit a high reversible capacity ($\sim 830 \text{ mA h g}^{-1}$ after 100 cycles, approximately 85% of theoretical capacity), and superior rate capability as anodes for Li-ion battery. Additionally, the electrochemical property of ZnO-based materials for Na-ion batteries is also proposed for the first time. It demonstrates that the as-synthesized ZnO/rGO/C composite also delivers an outperformance cyclic stability and considerable reversible capacity ($\sim 300 \text{ mA h g}^{-1}$ after 100 cycles). This simple methodology can be further extended to other energy storage applications.

Introduction

Considering the graveness of the environment issues and the shortage of energy source, lithium-ion batteries (LIBs) get much more attention with its large specific capacity, environmental friendliness, and long cycle life [1]. However, the capacity of the traditional graphite ($\sim 370 \text{ mA h g}^{-1}$) in theory is too low to meet the market demands. ZnO as one of the

transition metal oxides is widely utilized in many fields, such as organic light [2], gas sensors [3], and smartphone [4]. Especially, ZnO as a promising anode material can be utilized in LIBs due to the high theoretical capacity ($\sim 978 \text{ mA h g}^{-1}$) and good electrical conductivity. Nevertheless, the connatural high capacity of the ZnO is limited by a big volume change (the ZnO nanoparticles undergo 103% volume expansion after lithiation [5]) and the

Address correspondence to E-mail: ruizhao@uestc.edu.cn

aggregation of the formed ZnO during the long cycles. Aimed at the above issues, some promising approaches are used to improve ZnO anode materials for LIBs, including the thermal decomposition of $C_4H_4ZnO_6$ to ZnO@C [6], carbon/ZnO nanorod [7], ZnO-loaded/porous carbon [8], and $ZnCo_2O_4$ -ZnO nanorod arrays [9].

On the other hand, compared with the present Li-ion technologies, Na-ion batteries are becoming the promising candidates to meet the larger energy market demands, since the sodium materials have many practical advantages, such as low-cost and natural abundance [10]. However, lots of materials that can be well represented in the LIBs have bad performance in the Na-ion battery mainly due to the larger radius of the Na^+ than Li^+ . For example, graphite, as one of the frequently used electrode materials in LIBs, displays very poor capacity performance in the sodium-ion battery system [11]. In order to find the suitable electrode materials of the sodium-ion battery, it is believed that the bigger lattice constants and the open architectures of the as-prepared materials, such as the bowl-like hollow Co_3O_4 [12], porous $CoFe_2O_4$ nanocubes [13], porous CuO [14], and hierarchical durian-like NiS_2 [15] are beneficial to carry out a broad channel for the embedding of Na^+ .

Metal-organic frameworks (MOFs), representing a kind of special skeletal structure, are widely applied in gas storage [16], catalysis [17, 18], drug delivery [19], chemical sensing [20], and energy storage [21]. The MOFs materials are also used as electrode materials for LIBs owing to large surface areas and organized pore sizes [22], which conduce to making the anode contact with the more electrolyte and shortening the ion transport path. Besides, it has been demonstrated that the MOFs as the sacrificial templates can improve the structural stability of the electrode material during insertion and extraction of the ions [22–26]. The graphene nanosheets are broadly applied with the transition metal oxide as good buffers during the volume change in the long cycles and the perfect electrical conductors in the whole battery system [27–30].

In this work, we make MOFs as sacrificial templates with introducing the $Zn(NO_3)_2 \cdot 6H_2O$ and 2-methyl imidazole to fabricate ZnO-based nanoparticles. Additionally, GO and the glucose are imported as carbon sources. The construction of a suitable thin carbon layer on the ZnO/reduced graphene oxide

(ZnO/rGO) composite via a simple two-step methodology can efficiently utilize the advantage of this two carbon resources. The as-prepared ZnO/rGO/C composite can prevent the aggregation of ZnO, enhance the electronic conductivity and offer a robust scaffold during electrochemical processes with excellent electrochemical performance in LIBs. More importantly, the electrochemical property of ZnO-based materials for Na-ion batteries is also proposed for the first time. We believe this simple methodology can be widely used in other metal oxides system.

Experimental section

Preparation of GO

GO was prepared by Hummers method. In details, 180 ml of concentrated sulfuric acid, 20 ml of concentrated phosphoric acid, and 1.5 g of flake graphite were added into three flasks with slow mechanical agitation. And then, 9 g of $KMnO_4$ was slowly added into the mixed solution. The resulting mixture was further stirred at 48 °C for 12 h till the color of the mixture turned brown. H_2O_2 was added into the solution until the color became bright yellow and no more bubbles were formed. The mixture was centrifuged and washed with distilled water many times to remove excess acid and impurities, and the GO can be prepared by freeze-drying technique.

Preparation of ZnO, ZnO/rGO and ZnO/rGO/C

As for the MOFs and MOFs-GO, in briefly, 8 g of 2-methyl imidazole and the 3 g of $Zn(NO_3)_2 \cdot 6H_2O$ were dissolved in 25 ml methanol and 20 ml methanol, respectively. And then, 50 mg of graphene oxide powder was dissolved in 75 ml solution ($H_2O:CH_3CH_2OH = 1:2$). All of solutions were stirred for 0.5 h. Subsequently, the three kinds of solution were mixed together and stirred another 4 h. The resulting solution was centrifuged, washed with ethanol, and dried overnight at 80 °C in vacuum, and then the MOFs-GO was obtained. While the MOFs was synthesized by the same method without graphene, the ZnO was obtained by carbonizing MOFs at 650 °C for 2 h under N_2 protection directly. ZnO/rGO/C was synthesized by making the MOFs-GO as the template, and the 10 wt% glucose was utilized as the carbon

source to coat the MOFs-GO under the same condition as ZnO. The ZnO/rGO was formed in the same process without adding glucose. The synthetic routes of ZnO, ZnO/rGO, and ZnO/rGO/C are demonstrated in Fig. 1.

Sample characterizations

The thermogravimetric analysis (TGA) and differential scanning calorimetry (DSC) were recorded on a NETZSCH STA 409 PC/DSC. Using JSM, 6490LV and NavoNano Eml to obtain scanning electron microscope (SEM) images, transmission electron microscope (TEM) images were carried out on a JSM 64090LV transmission electron microscope. A Rigaku RINT 2400 X-ray diffractometer with Cu K α radiation was used to collect X-ray diffraction (XRD) patterns. The Brunauer–Emmett–Teller (BET) and Barrett–Joyner–Halenda (BJH) were performed on a ASAP2020.

Electrochemical testing

The working electrode contains 80 wt% active materials, 10 wt% acetylene black and 10 wt% polyvinylidene difluoride (PVDF). For LIBs, a CR2032 coin-type half-cell was assembled with Celgard 2500 as the separator, the lithium foil as the counter electrode, and 1.0 M LiPF₆ solution in ethylene carbonate (EC): diethyl carbonate (DEC):

dimethyl carbonate (DMC) (1:1:1) as the electrolyte. For assembling sodium cells, the sodium foil was used as the reference electrode and 1 M NaPF₆ in EC: DMC (1:1) as the electrolyte, and the glasses fiber as the separator.

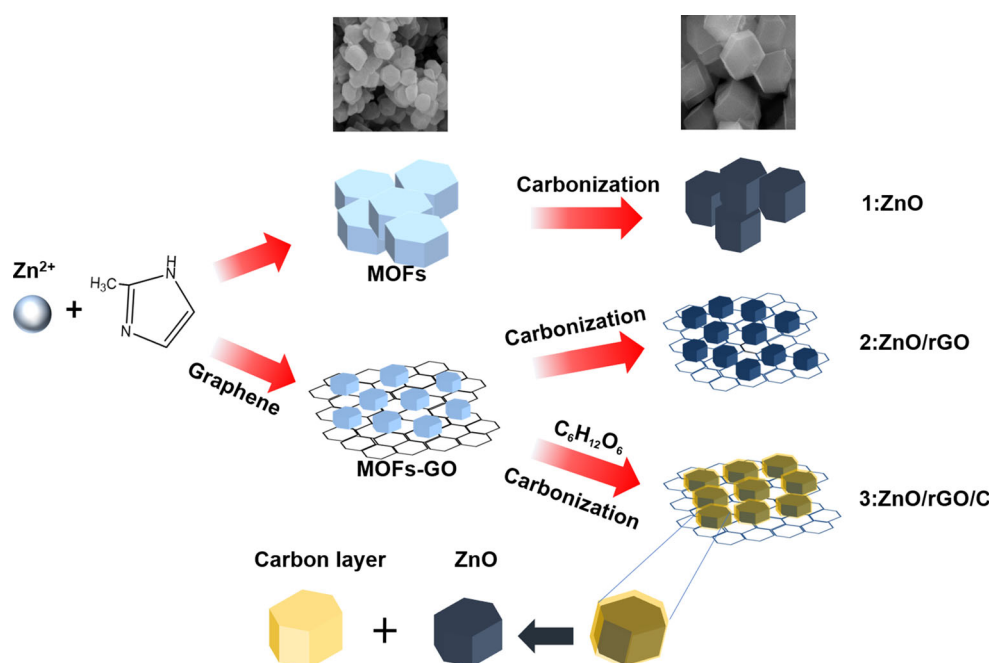
The galvanostatic charge–discharge test was carried out with a LAND system with the cutoff potential window between 0.01 and 3 V for Li-ion batteries, between 0.01 and 2.5 V for Na-ion batteries, respectively. And cyclic voltammetry (CV) tests were measured on Chenghua CHI 660E for Li-ion batteries between 0.01 and 3.0 V with a scan rate of 0.1 mV s⁻¹, while the Na-ion batteries between 0.01 and 2.5 V with a scan rate of 0.05 mV s⁻¹. The electrochemical impedance spectroscopy (EIS) was performed on the frequency ranging from 100 kHz to 0.01 Hz on a Chenghua CHI 660E electrochemical station.

Results and discussion

Structure and morphology

The as-prepared ZnO-based composites were identified by XRD. Figure 2 shows the XRD patterns of ZnO/rGO/C, ZnO/rGO, and ZnO. Clear diffraction peaks at 31.64°, 34.13°, 36.28°, 47.52°, 56.7°, 63.05°, 66.32°, 67.89°, and 69.29° can be observed for all the samples, corresponding to (100), (002), (101), (102),

Figure 1 The synthesizing processes of the ZnO, ZnO/rGO, and ZnO/rGO/C. (1) the bare ZnO was obtained by carbonizing MOFs. (2) MOFs-GO was carbonized to get the ZnO/rGO. (3) ZnO/rGO/C was obtained by carbonizing MOFs-GO and C₆H₁₂O₆ together.



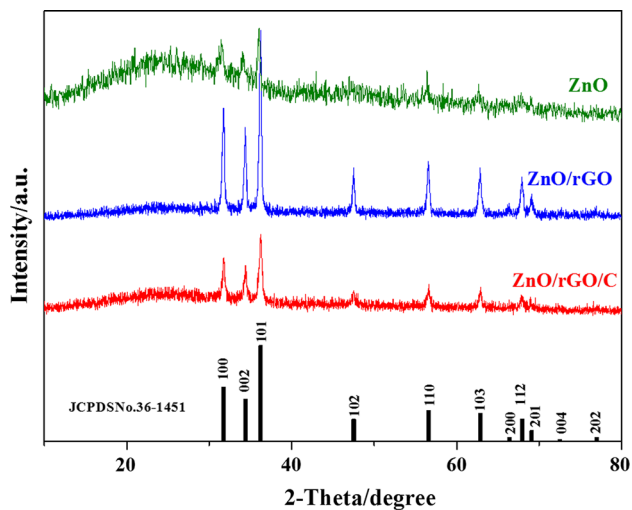


Figure 2 XRD patterns of as-prepared ZnO, ZnO/rGO, and ZnO/rGO/C.

(110), (103), (200), (112), and (201) planes of hexagonal prisms ZnO (JCPDS No. 36-1451), respectively. It suggests the presence of ZnO crystals without obvious impurity in all three samples. An arc peak of ZnO pattern is observed at $\sim 25^\circ$, which can be related to the carbon produced by the pyrolysis of MOFs [31]. Moreover, the typical diffraction peak at $\sim 11^\circ$ for graphene sheets cannot be obviously distinguished in the XRD patterns of the ZnO/rGO/C and ZnO/rGO, which may be ascribed to the reduction in the GO [32].

The morphology and microstructure of ZnO/rGO/C, ZnO/rGO, and ZnO composites were examined by SEM. The bare ZnO synthesized with the same procedure without GO and $C_6H_{12}O_6$ is revealed in Fig. 3a, d. A great deal of homogeneous ZnO nanoparticles is dispersed on reduced graphene sheets as shown in Fig. 3b, f. These ZnO nanoparticles are around 80–150 nm in size with hexahedron frame structure and can form an alternating lamellar structure with rGO nanosheets. This unique stabilized frame structure can play a significant role in the process of insertion and extraction of Li^+ or Na^+ , which can improve the electrochemical performance during the long cycles.

In order to further explore the structural information of ZnO/rGO/C, the as-prepared material was identified by TEM and HRTEM characterizations. ZnO nanoparticles with the size about 180 nm (Fig. 4a) were coated with an amorphous carbon layer with the thickness of several nanometers, which can also be in well agreement with Fig. 4b. Besides, as

shown in Fig. 4c, these nanoparticles were dispersed on reduced graphene nanosheets. It can be concluded that the structure: ZnO-based MOFs were coated with a layer of carbon and dispersed on rGO sheets successfully, and the special structure can correspond to what we originally designed (Fig. 4f). Furthermore, Fig. 4d, e shows the fringe spacing of the lattice is 0.28 and 0.19 nm, corresponding to the lattice plane of (100) and (102) of ZnO, respectively.

The content of active materials in the composite was measured by thermogravimetric analysis (TGA) and differential scanning calorimetry (DSC) in the air. From Fig. 5a, there is a visible weight loss for ZnO/rGO over the temperature range from 100 to $450^\circ C$. At the same time, there is a strong endothermic peak at $454.4^\circ C$, which can be attributed to the gradual decomposition of the organic matter of ZnO/rGO. From 454.5 to $562.1^\circ C$, a substantial loss of weight may correspond to the combustion of carbon in the air [8]. With the temperature increasing, the weight loss is finished at around $600^\circ C$. Therefore, the weight percentage of ZnO in ZnO/rGO and ZnO/rGO/C were calculated to be 53.78 and 47.39%, respectively.

The specific surface area and pore size distribution of these three samples were obtained by using Brunauer–Emmett–Teller (BET) and Barrett–Joyner–Halenda (BJH) methods at 77 K. The nitrogen absorption–desorption isotherms of Fig. 5c show that the isotherm curves of the ZnO/rGO display a obvious Langmuir IV behavior with the H3-type hysteresis loop at a relative pressures of 0.4–0.9, which indicates that the mesoporous exists in it [33]. While the nitrogen-adsorption curves of ZnO and ZnO/rGO/C show that both of them are microporous structure. The BET specific surface area of ZnO/rGO/C ($128.33\text{ m}^2\text{ g}^{-1}$) is lower than that of ZnO/rGO ($151.08\text{ m}^2\text{ g}^{-1}$), mainly due to the thin carbon layer coated on the composites. And the BET specific surface area of the ZnO is only $31.96\text{ m}^2\text{ g}^{-1}$ due to the agglomeration of ZnO nanoparticles in the absence of GO nanosheets. The pore size distributions of ZnO, ZnO/rGO, and ZnO/rGO/C are shown in Fig. 5d.

Lithium storage performance

The CV and the initial three charge–discharge curves of the as-prepared three ZnO-containing samples between 0.01 and 3 V are shown in Fig. 6. Due to the

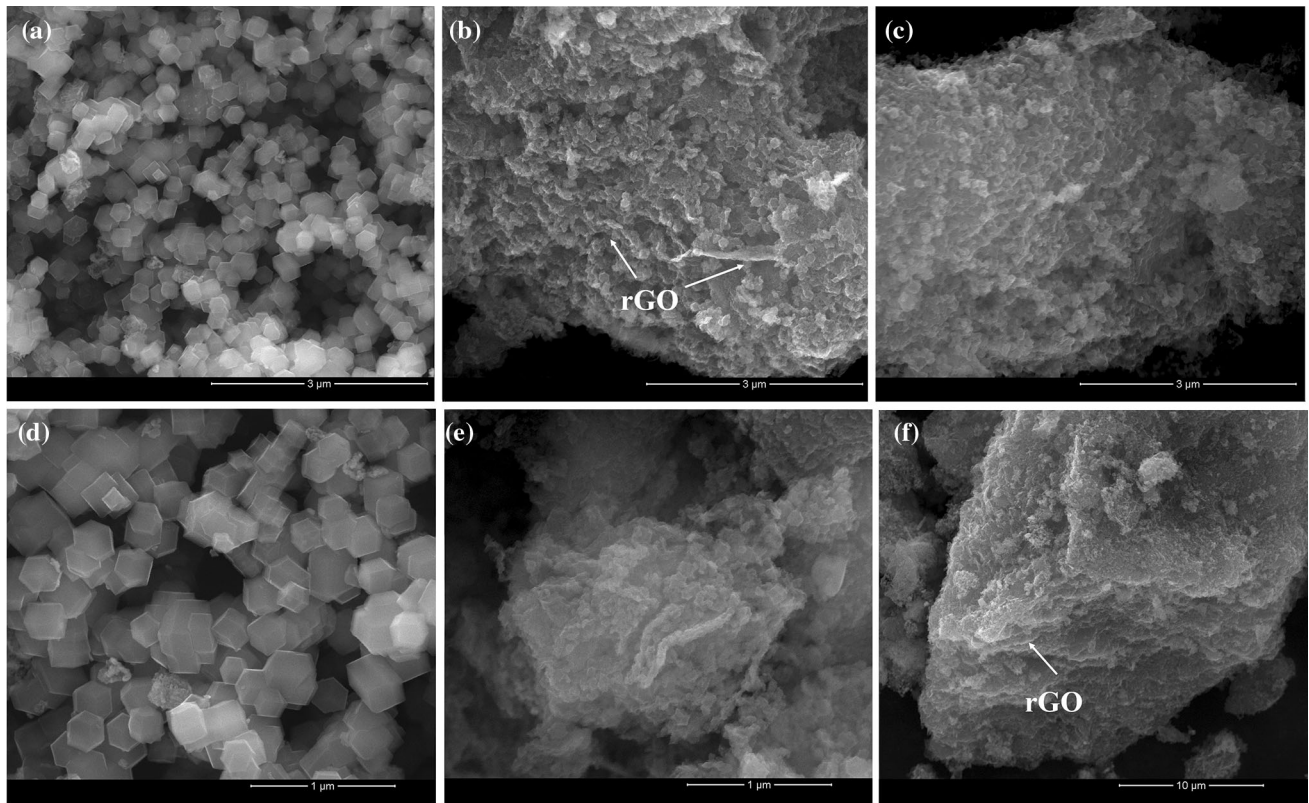


Figure 3 SEM images of the ZnO-based samples. **a, d** the bare ZnO, **b, e** ZnO/rGO, and **c, f** ZnO/rGO/C composite with different magnifications.

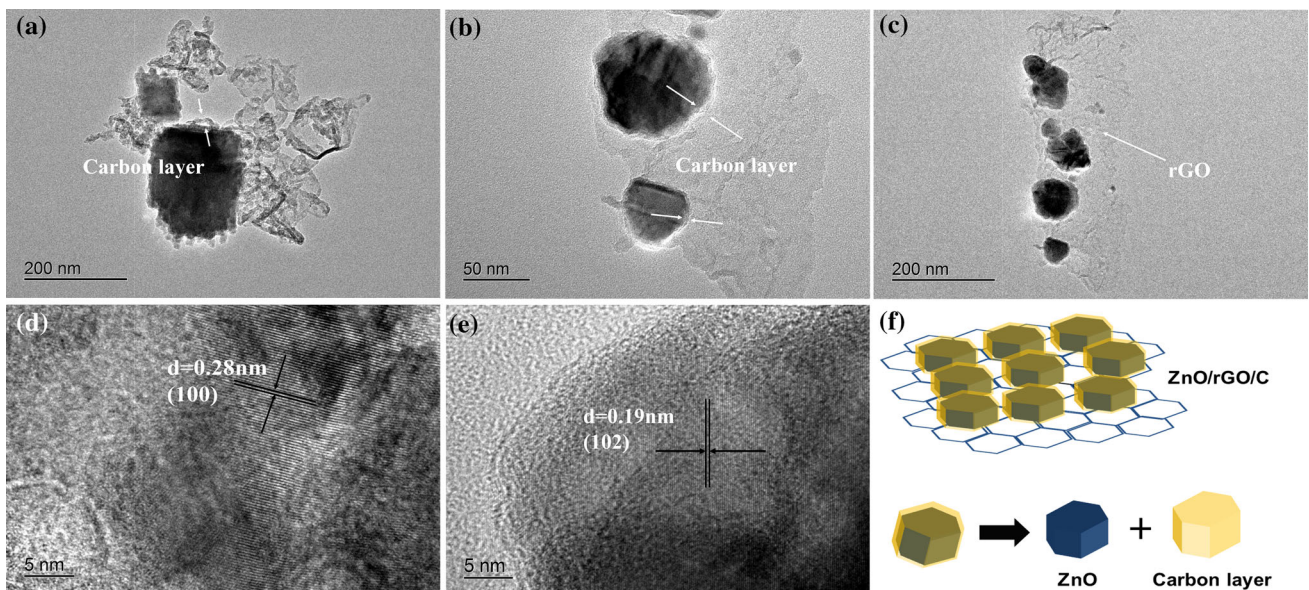


Figure 4 **a, b, c** TEM images of the ZnO/rGO/C, **d, e** HRTEM images of ZnO/rGO/C, and **f** schematic diagram of ZnO/rGO/C.

aggregation and poor electronic conductivity of ZnO nanoparticles, the bare ZnO sample shows weak reversible peaks in its CV curve and poor

electrochemical property as anode for Li-ion batteries (shown in Fig. 6a, d). Nevertheless, for the modified ZnO/rGO composite in Fig. 6b, during the first

Figure 5 DSC and TGA curves of **a** ZnO/rGO, **b** ZnO/rGO/C in the air, **c** N₂ adsorption–desorption isotherms, and **d** the pore size distribution of the bare ZnO, ZnO/rGO, and ZnO/rGO/C.

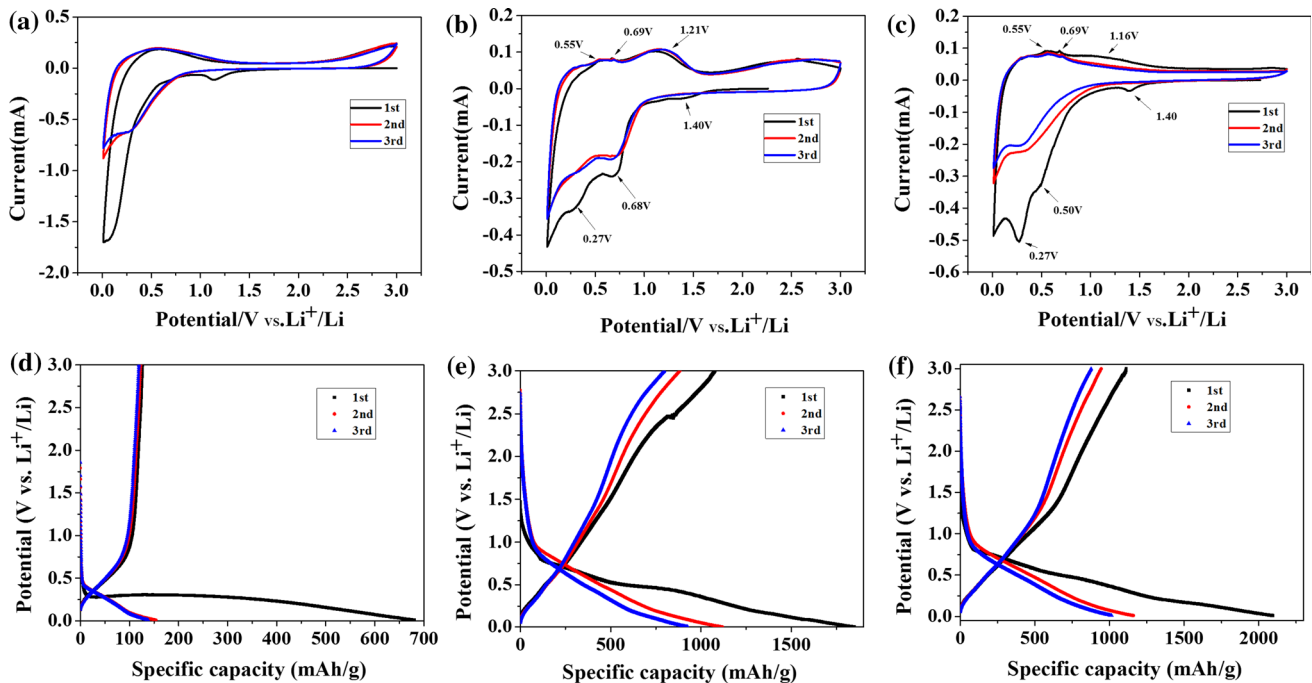
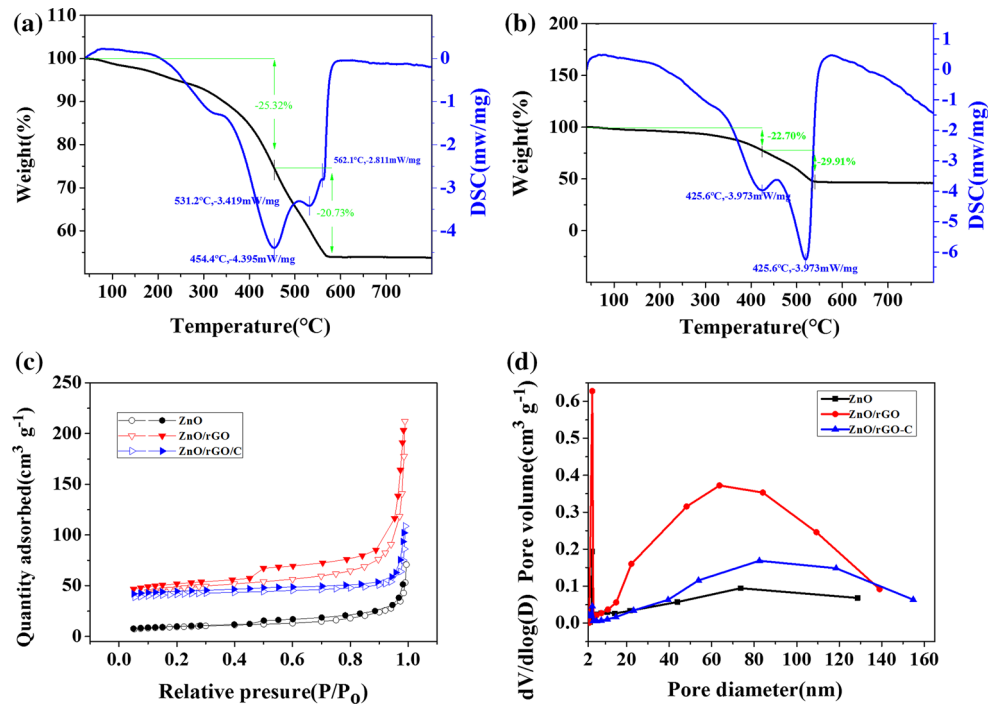


Figure 6 The CV curves of **a** ZnO, **b** ZnO/rGO, and **c** ZnO/rGO/C at a scan rate of 0.1 mV s⁻¹. The charge/discharge profiles of **d** ZnO, **e** ZnO/rGO, and **f** ZnO/rGO/C during the first three cycles.

lithiation process, two distinct reduction peaks appeared at 0.27 and 0.68 V, which are related to the reduction of the ZnO to Zn, Zn to the Li-Zn alloy, and the formation of solid electrolyte interface (SEI) [34]. A reduction peak appeared at 1.40 V, but

disappeared in the rest of cycles, which is assigned to the formation of the irreversible Li₂O. In the first delithiation process, three peaks at 0.55, 0.69, and 1.21 V were observed, indicating the dealloying processes of Li-Zn alloys [35]. The CV curves of the

ZnO/rGO/C in Fig. 6c were similar to those of ZnO/rGO. Moreover, the curves of CV are highly coincident over the next few cycles, demonstrating the good reversibility of the ZnO/rGO and ZnO/rGO/C. The first coulombic efficiency (CE) of ZnO ($\sim 18.6\%$) is lower than the ZnO/rGO ($\sim 58.3\%$) and ZnO/rGO/C ($\sim 53.1\%$). The rather low initial CE for bare ZnO is caused by the formation of SEI layer, its poor electronic conductivity as well as the aggregation. The CE of ZnO/rGO is slightly higher than the ZnO/rGO/C mainly due to the electrochemical reaction between carbon and lithium in the first cycle. Obviously, both the ZnO/rGO (Fig. 6e) and ZnO/rGO/C (Fig. 6f) can deliver better specific discharge/charge capacity than the bare ZnO, mainly due to the well-defined structure composed of rGO nanosheets that play a very favorable role during electrochemical processes [36].

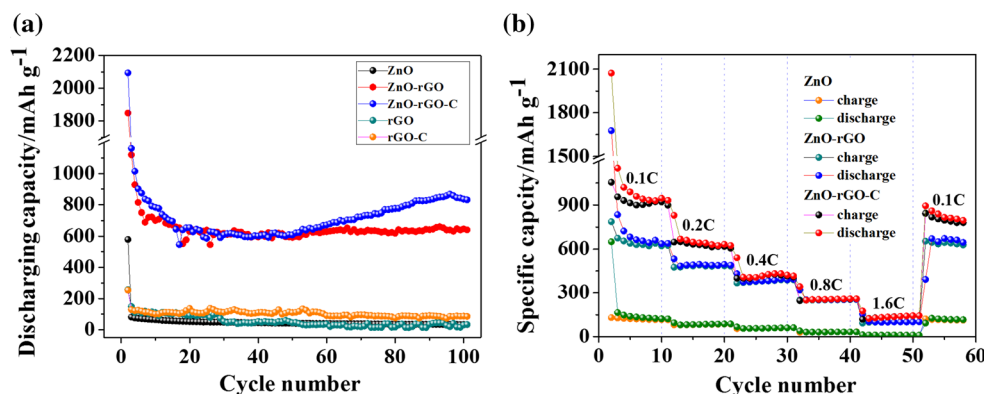
The cyclic behaviors of the ZnO, ZnO/rGO, and ZnO/rGO/C at 0.1C ($1C = 978 \text{ mA g}^{-1}$) are shown in Fig. 7a. The reversible capacity of ZnO/rGO/C decreased slightly in the initial 20 cycles and then increased gradually during the rest of cycles, which should be related the activation of the electrodes since a part of the capacity was released from the surface layer of the polymer [37, 38]. And then it reaches its highest value of 878 mA h g^{-1} in the 95th cycle, followed by a slow decline with 830 mA h g^{-1} of capacity retained after 100 cycles. The ZnO/rGO/C exhibits the superior cycling behaviors and higher reversible capacities ($\sim 830 \text{ mA h g}^{-1}$) than the ZnO/rGO ($\sim 640 \text{ mA h g}^{-1}$) and the bare ZnO ($\sim 100 \text{ mA h g}^{-1}$), which are ascribed to its optimal morphologies and special structures. Namely, (1) the metal–organic frameworks of the composite can buffer the volume expansion during the insertion and extraction of Li^+ ; (2) the reduced graphene can

contribute to dispersing the composite nanoparticles and prevent them from aggregation; and (3) the amorphous carbon layers, which coat the hexahedron ZnO composites, not only can amortize the large volume change, enhance the electrical conductivity of the as-prepared materials, but also prevent the falling off of electrode capacity during the charge–discharge processes [8]. These favorable factors produce synergistic effects, resulting in the excellent charge–discharge performance of ZnO/rGO/C.

To exclude the contribution of rGO and carbon layer to the capacity of Li-ion batteries systems, we prepared rGO, rGO/C under the same conditions to assemble Li-ion batteries without the $\text{Zn}(\text{NO}_3)_2 \cdot 6\text{H}_2\text{O}$ and 2-methyl imidazole. From Fig. 7a, the capacity of rGO was only 22 mA h g^{-1} after 100 cycles, which can be ascribed to the amorphous structure of the as-prepared rGO. This amorphous form of rGO mainly prevents the agglomeration of nanoparticles with ignorable capacity contribution during charging and discharging processes. As shown in Fig. 7a, the rGO/C displays a capacity of $\sim 90 \text{ mA h g}^{-1}$ after one hundred cycles, and the carbon layer can sustain the structure during the long cycles [8].

The rate capability of ZnO, ZnO/rGO, and ZnO/rGO/C was evaluated at 0.1–1.6 C as shown in Fig. 7b. Compared to the ZnO, the ZnO/rGO composite shows a better rate performance, which is related to the good electronic conductivity and the shorter Li-ion transport path of ZnO/rGO. Notably, the ZnO/rGO/C composite displays the best electrochemical property. To be specific, the reversible capacity of ZnO/rGO/C was $\sim 154 \text{ mA h g}^{-1}$ at 1.6C, much higher than those of ZnO/rGO ($\sim 93 \text{ mA h g}^{-1}$) and ZnO ($\sim 17 \text{ mA h g}^{-1}$). In addition, ZnO/rGO/C can recover a capacity of 830 mA h g^{-1} when the current rate is back to 0.1 C,

Figure 7 **a** The specific capacities of ZnO, ZnO/rGO, ZnO/rGO/C, rGO, and rGO/C at 0.1 C, **b** the rate capability of ZnO, ZnO/rGO, and ZnO/rGO/C at different current density.



exhibiting an excellent rate performance, which is mainly due to its optimal morphologies and special carbon-coating structure. In other words, the reducing graphene and carbon not merely promote the electronic conductivity, but increase the contact area with the electrolyte, and short the Li^+ diffusion pathway.

To get a better insight into electrochemical behaviors of Li-ion system for the ZnO-based composites, the EIS of the three samples electrodes before and after 100 cycles is tested in Fig. 8. An arc shape at the high frequency which is related to the charge transfer resistance (R_{ct}) and SEI film resistance (R_{sf}) at the interface between electrode and electrolyte. In the low frequency, the line can correspond to the resistance of the process of Li^+ diffusion with electrodes. The resistance sums (R_{sf+ct}) of the ZnO/rGO/C, ZnO/rGO, and ZnO in Li-ion half-cell were estimated to be 96, 100, and 114 Ω , and shifted to 68, 153, and 419 Ω after 100 cycles, respectively, indicating the ZnO/rGO/C composite displays the highest electrochemical activity and the excellent reaction kinetics. Moreover, the unique structure made up of rGO and carbon layers can enhance electronic conductivity and shorten Li-ion transport pathway.

Sodium storage performance

To study the role of these materials in other types of batteries, the ZnO/rGO/C, ZnO/rGO and ZnO were

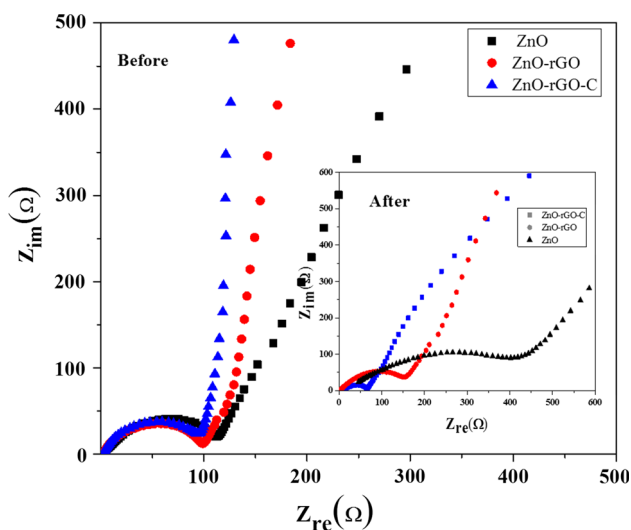
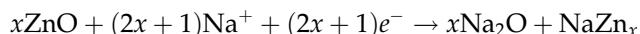


Figure 8 EIS of the fresh ZnO, ZnO/rGO, and ZnO/rGO/C electrode. (inset is the electrode after 100 cycles for the three samples).

also newly applied as anode materials for Na-ion batteries. The cutoff voltage is between 0.01 and 2.5 V. As shown in Fig. 9a, the first CE of ZnO/rGO/C is 32.9%, which may be related to the bigger radius of sodium and the irreversible damage of electrode in the first sodiation process [39]. Besides, the first CE of ZnO/rGO/C is higher than that of ZnO/rGO ($\sim 22.8\%$) and the ZnO ($\sim 3.6\%$) in sodium battery systems, and it should be ascribed to the strong frameworks and the well-defined transport channels of ZnO/rGO/C.

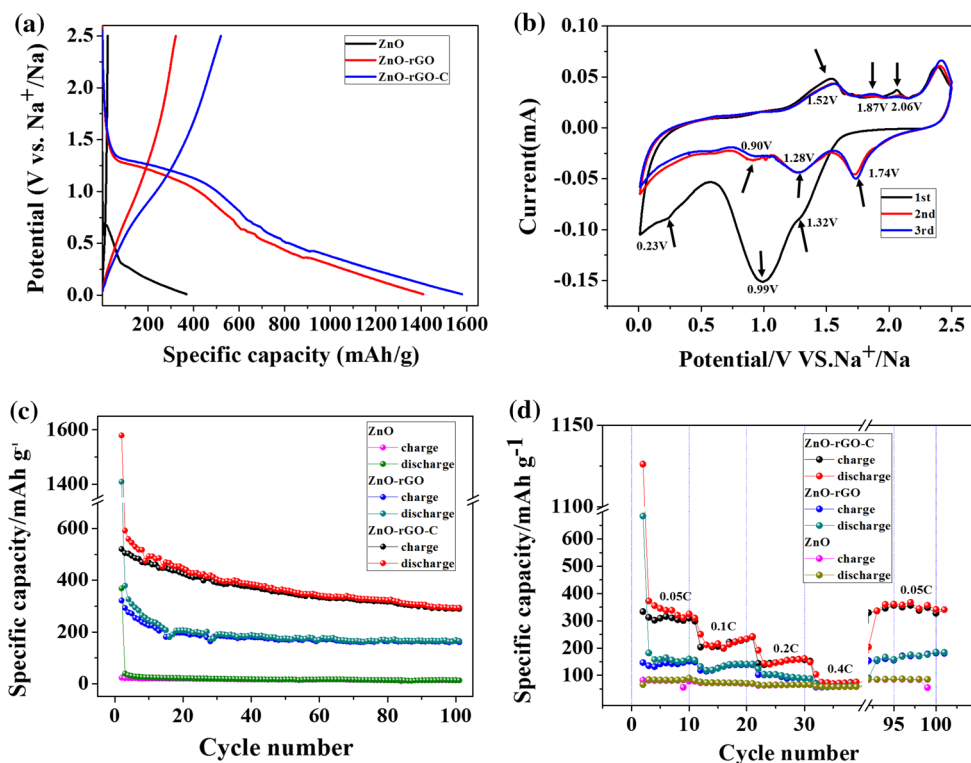
To understand the reaction mechanism of ZnO in Na-ion battery, Fig. 9b shows the first three CV curves of the ZnO/rGO/C electrode at room temperature between 0.01 and 2.5 V at a scan rate of 0.05 mV s^{-1} . In the first sodiation process, the three distinct cathodic peaks were observed at voltages of 0.23, 0.99, and 1.23 V, which is related to the electrochemical conversion of ZnO to Zn, Zn to NaZn_x , and the formation of Na_2O and SEI layer. In the subsequent cycles, these cathodic peaks were shifted higher to 0.9, 1.28, and 1.74 V due to the polarization effect, respectively. The electrochemical process and the reformation of ZnO can be demonstrated by the following electrochemical conversion reaction [39]:



In the initial desodiation process, three distinct peaks can be observed at 1.52, 1.87, and 2.06 V, which can be related to the dealloying of NaZn_x to Zn, re-oxidation of Zn to ZnO, and decomposition of Na_2O . In following CV cycles, the overlap of both oxidation curves and reduction curves confirms the high reversibility of Na_2O and NaZn_x again.

ZnO/rGO/C composites exhibit the best behavior performance among these three materials in Fig. 9c. Compared with the Li-ion batteries, the first discharge capacity ($1579.6 \text{ mA h g}^{-1}$) of Na-ion batteries is lower, which should be ascribed to bigger radius of Na^+ than Li^+ . However, even the radius of Na^+ is 34.2% bigger than that of Li^+ , the unique structure of ZnO/rGO/C still accommodates the insertion of Na^+ . The capacity retention can be maintained at 300 mA h g^{-1} after 100 cycles is higher than that of ZnO ($\sim 13 \text{ mA h g}^{-1}$) and ZnO/rGO ($\sim 164 \text{ mA h g}^{-1}$), thus outperforms many of the transition metal oxide materials for SIBs [12–14, 40, 41].

Figure 9 **a** The first charge–discharge curves of ZnO, ZnO/rGO, and ZnO/rGO/C, **b** the CV curves of ZnO/rGO/C anodes at 0.05 C in sodium-ion systems, **c** the discharge–charge capacities, and **d** rate behavior of all three anodes.



In addition, this is the first time using the as-prepared material as anode materials of SIBs as far as we know. The rate performance of the as-prepared materials was also evaluated in Fig. 9d. Among three kinds of anode materials, the ZnO/rGO/C has the best rate capability and optimal reversibility, the reversible capacity of ZnO/rGO/C was $\sim 162 \text{ mA h g}^{-1}$ at 0.2C, much higher than those of ZnO/rGO ($\sim 101 \text{ mA h g}^{-1}$) and ZnO ($\sim 60 \text{ mA h g}^{-1}$) in SIBs. When the current density reverses back to 0.05C, the capacity of the ZnO/rGO/C still remains 342 mA h g^{-1} after 100 cycles. Furthermore, this new synthesis method can be further extended to other secondary batteries, and the related work is still ongoing.

Conclusions

In summary, a novel ZnO/reduced graphene oxide/carbon composite is synthesized successfully via a simple pyrolysis of Zn-based metal–organic framework. This special structure is made of ZnO which is homogeneously dispersed on rGO sheets and coated with a carbon layer. It exhibits superior rate capability, especially reversible capacity

($\sim 830 \text{ mA h g}^{-1}$ after 100 cycles, approximately 85% of theoretical capacity) as anodes for LIBs. Additionally, it is the first time to use ZnO materials as anodes for Na-ion battery, and it demonstrates an outperformance cyclic stability and considerable reversible capacity ($\sim 300 \text{ mA h g}^{-1}$ after 100 cycles). The special structure, herein, not only can amortize the large volume change, enhance the electrical conductivity, but also prevent the falling off of electrode capacity. This simple method of synthesizing this unique structure can be widely applied in energy storage materials and extended to other important applications.

Acknowledgements

This work was financially supported by Science Foundation of Xi'an University of Technology in China No. 101-451117007 and Natural Science Foundation of China (NSFC No. 51707153).

References

- [1] Armand M, Tarascon JM (2008) Building better batteries. *Nature* 451:652–657. <https://doi.org/10.1038/451652a>

- [2] Wang H, Li K, Tao Y et al (2017) Smooth ZnO:Al-AgNWs composite electrode for flexible organic light-emitting device. *Nanoscale Res Lett* 12:77–83. <https://doi.org/10.1186/s11671-017-1841-2>
- [3] Skompska M, Zarebska K (2014) Electrodeposition of ZnO nanorod arrays on transparent conducting substrates—a review. *Electrochim Acta* 127:467–488. <https://doi.org/10.1016/j.electacta.2014.02.049>
- [4] Liu L, Zhang D, Zhang Q et al (2017) Smartphone-based sensing system using ZnO and graphene modified electrodes for VOCs detection. *Biosens Bioelectron* 93:94–101. <https://doi.org/10.1016/j.bios.2016.09.084>
- [5] Wang H, Pan Q, Cheng Y, Zhao J, Yin G (2009) Evaluation of ZnO nanorod arrays with dandelion-like morphology as negative electrodes for lithium-ion batteries. *Electrochim Acta* 54:2851–2855. <https://doi.org/10.1016/j.electacta.2008.11.019>
- [6] Wei D, Xu Z, Wang J et al (2017) A one-pot thermal decomposition of $C_4H_4ZnO_6$ to ZnO@carbon composite for lithium storage. *J Alloy Compd* 714:13–19. <https://doi.org/10.1016/j.jallcom.2017.04.214>
- [7] Liu J, Li Y, Ding R et al (2009) Carbon/ZnO nanorod array electrode with significantly improved lithium storage capability. *J Phys Chem C* 113:5336–5339. <https://doi.org/10.1021/jp9034612>
- [8] Shen X, Mu D, Chen S, Wu B, Wu F (2013) Enhanced electrochemical performance of ZnO-loaded/porous carbon composite as anode materials for lithium ion batteries. *Acs Appl Mater Interfaces* 5:3118–3125. <https://doi.org/10.1021/am400020n>
- [9] Gan QM, Zhao KM, Liu SQ, He Z (2017) MOF-derived carbon coating on self-supported $ZnCo_2O_4$ -ZnO nanorod arrays as high-performance anode for lithium-ion batteries. *J Mater Sci* 52:7768–7780. <https://doi.org/10.1007/s10853-017-1043-4>
- [10] Ning Y, Lou X, Shen M, Hu B (2017) Mesoporous cobalt 2,5-thiophenedicarboxylic coordination polymer for high performance Na-ion batteries. *Mater Lett* 197:245–248. <https://doi.org/10.1016/j.matlet.2017.01.126>
- [11] Slater MD, Kim D, Lee E, Johnson CS (2013) Sodium-ion batteries. *Adv Funct Mater* 23:947–958. <https://doi.org/10.1002/adfm.201200691>
- [12] Wen J-W, Zhang D-W, Zang Y et al (2014) Li and Na storage behavior of bowl-like hollow Co_3O_4 microspheres as an anode material for lithium-ion and sodium-ion batteries. *Electrochim Acta* 132:193–199. <https://doi.org/10.1016/j.electacta.2014.03.139>
- [13] Zhang X, Li D, Zhu G, Lu T, Pan L (2017) Porous $CoFe_2O_4$ nanocubes derived from metal–organic frameworks as high-performance anode for sodium ion batteries. *J Colloid Interface Sci* 499:145–150. <https://doi.org/10.1016/j.jcis.2017.03.104>
- [14] Li D, Yan D, Zhang X, Li J, Lu T, Pan L (2017) Porous CuO/reduced graphene oxide composites synthesized from metal–organic frameworks as anodes for high-performance sodium-ion batteries. *J Colloid Interface Sci* 497:350–358. <https://doi.org/10.1016/j.jcis.2017.03.037>
- [15] Zhu KJ, Liu G, Wang YJ et al (2017) Metal-organic frameworks derived novel hierarchical durian-like nickel sulfide (NiS_2) as an anode material for high-performance sodium-ion batteries. *Mater Lett* 197:180–183. <https://doi.org/10.1016/j.matlet.2017.03.087>
- [16] Rosi NL, Eckert J, Eddaoudi M et al (2003) Hydrogen storage in microporous metal-organic frameworks. *Science* 300:1127–1129
- [17] Zhu Q-L, Li J, Xu Q (2013) Immobilizing metal nanoparticles to metal–organic frameworks with size and location control for optimizing catalytic performance. *J Am Chem Soc* 135:10210–10213. <https://doi.org/10.1021/ja403330m>
- [18] Lee J, Farha OK, Roberts J, Scheidt KA, Nguyen ST, Hupp JT (2009) Metal-organic framework materials as catalysts. *Chem Soc Rev* 38:1450–1459. <https://doi.org/10.1039/b807080f>
- [19] Ke F, Yuan Y-P, Qiu L-G et al (2011) Facile fabrication of magnetic metal–organic framework nanocomposites for potential targeted drug delivery. *J Mater Chem* 21:3843–3848
- [20] Pramanik S, Zheng C, Zhang X, Emge TJ, Li J (2011) New microporous metal–organic framework demonstrating unique selectivity for detection of high explosives and aromatic compounds. *J Am Chem Soc* 133:4153–4155
- [21] Ge L, Zhou W, Rudolph V, Zhu Z (2013) Mixed matrix membranes incorporated with size-reduced Cu-BTC for improved gas separation. *J Mater Chem A* 1:6350–6358. <https://doi.org/10.1039/c3ta11131h>
- [22] Lee KJ, Kim T-H, Kim TK, Lee JH, Song H-K, Moon HR (2014) Preparation of Co_3O_4 electrode materials with different microstructures via pseudomorphic conversion of Co-based metal-organic frameworks. *J Mater Chem A* 2:14393–14400. <https://doi.org/10.1039/c4ta02501f>
- [23] Zhang L, Yan B, Zhang J, Liu Y, Yuan A, Yang G (2016) Design and self-assembly of metal–organic framework-derived porous Co_3O_4 hierarchical structures for lithium-ion batteries. *Ceram Int* 42:5160–5170. <https://doi.org/10.1016/j.ceramint.2015.12.038>
- [24] Park KS, Ni Z, Côté AP et al (2006) Exceptional chemical and thermal stability of zeolitic imidazolate frameworks. *Proc Natl Acad Sci* 103:10186–10191
- [25] Huang G, Zhang L, Zhang F, Wang L (2014) Metal–organic framework derived $Fe_2O_3@NiCo_2O_4$ porous nanocages as

- anode materials for Li-ion batteries. *Nanoscale* 6:5509–5515. <https://doi.org/10.1039/c3nr06041a>
- [26] Huang G, Zhang F, Du X, Qin Y, Yin D, Wang L (2015) Metal organic frameworks route to in situ insertion of multiwalled carbon nanotubes in Co_3O_4 polyhedra as anode materials for lithium-ion batteries. *ACS Nano* 9:1592–1599. <https://doi.org/10.1021/nn506252u>
- [27] Jing Y, Zhou Z, Cabrera CR, Chen Z (2014) Graphene, inorganic graphene analogs and their composites for lithium ion batteries. *J Mater Chem A* 2:12104–12122. <https://doi.org/10.1039/c4ta01033g>
- [28] Lv D, Gordin ML, Yi R et al (2014) GeO_x /Reduced graphene oxide composite as an anode for li-ion batteries: enhanced capacity via reversible utilization of Li_2O along with improved rate performance. *Adv Func Mater* 24:1059–1066. <https://doi.org/10.1002/adfm.201301882>
- [29] Zhen M, Guo S, Gao G, Zhou Z, Liu L (2015) TiO_2 -B nanorods on reduced graphene oxide as anode materials for Li ion batteries. *Chem Commun* 51:507–510. <https://doi.org/10.1039/c4cc07446g>
- [30] Yu S-H, Conte DE, Baek S et al (2013) Structure-properties relationship in iron oxide-reduced graphene oxide nanostructures for li-ion batteries. *Adv Func Mater* 23:4293–4305. <https://doi.org/10.1002/adfm.201300190>
- [31] Tang J, Yamauchi Y (2016) Carbon Materials MOF morphologies in control. *Nat Chem* 8:638–639. <https://doi.org/10.1038/nchem.2548>
- [32] Guo R, Yue WB, An YM, Ren Y, Yan X (2014) Graphene-encapsulated porous carbon-ZnO composites as high-performance anode materials for Li-ion batteries. *Electrochim Acta* 135:161–167. <https://doi.org/10.1016/j.electacta.2014.04.160>
- [33] Chen JS, Zhu T, Hu QH et al (2010) Shape-controlled synthesis of cobalt-based nanocubes, nanodiscs, and nanoflowers and their comparative lithium-storage properties. *ACS Appl Mater Interfaces* 2:3628–3635. <https://doi.org/10.1021/am100787w>
- [34] Zhou Z, Zhang K, Liu J, Peng H, Li G (2015) Comparison study of electrochemical properties of porous zinc oxide/N-doped carbon and pristine zinc oxide polyhedrons. *J Power Sour* 285:406–412
- [35] Chae OB, Park S, Ryu JH, Oh SM (2013) Performance improvement of nano-sized zinc oxide electrode by embedding in carbon matrix for lithium-ion batteries. *J Electrochem Soc* 160:A11–A14. <https://doi.org/10.1149/2.024301jes>
- [36] Zhou G, Wang D-W, Li F et al (2010) Graphene-wrapped Fe_3O_4 anode material with improved reversible capacity and cyclic stability for lithium ion batteries. *Chem Mater* 22:5306–5313. <https://doi.org/10.1021/cm101532x>
- [37] Shaju KM, Jiao F, Debart A, Bruce PG (2007) Mesoporous and nanowire Co_3O_4 as negative electrodes for rechargeable lithium batteries. *Phys Chem Chem Phys* 9:1837–1842. <https://doi.org/10.1039/b617519h>
- [38] Wang L, Schnepf Z, Titirici MM (2013) Rice husk-derived carbon anodes for lithium ion batteries. *J Mater Chem A* 1:5269–5273
- [39] Xu F, Li Z, Wu L et al (2016) In situ TEM probing of crystallization form-dependent sodiation behavior in ZnO nanowires for sodium-ion batteries. *Nano Energy* 30:771–779. <https://doi.org/10.1016/j.nanoen.2016.09.020>
- [40] Wang Y, Wang C, Wang Y, Liu H, Huang Z (2016) Superior sodium-ion storage performance of Co_3O_4 @ nitrogen-doped carbon: derived from a metal-organic framework. *J Mater Chem A* 4:5428–5435
- [41] Klein F, Pinedo R, Berkes BB, Janek J, Adelhelm P (2017) Kinetics and degradation processes of CuO as conversion electrode for sodium-ion batteries: an electrochemical study combined with pressure monitoring and DEMS. *J Phys Chem C* 121:8679–8691. <https://doi.org/10.1021/acs.jpcc.6b11149>